Composites: Part A 180 (2024) 108084

Contents lists available at ScienceDirect

Composites Part A

journal homepage: www.elsevier.com/locate/compositesa

Through-thickness frontal polymerization: Process development and optimization

S. Vyas [a,b,1], N.A. Parikh [a,b,1], T.C. Price [a,c], D.P. Patel [a,b], T.B. Le [a,b], P.H. Geubelle [a,b,*], N.R. Sottos [a,c,**]

[a] Beckman Institute for Advanced Science and Technology, University of Illinois Urbana Champaign, Urbana, IL 61801, United States
[b] Department of Aerospace Engineering, University of Illinois Urbana Champaign, Urbana, IL 61801, United States
[c] Department of Materials Science Engineering, University of Illinois Urbana Champaign, Urbana, IL 61801, United States

ARTICLE INFO

Keywords:
Frontal polymerization (E)
Carbon fibers (A)
Polymer-matrix composites (A)
Modeling (C)

ABSTRACT

Current methods for the manufacture of fiber-reinforced polymer composites (FRPCs) are energy intensive, time consuming, and have adverse effects on the environment. Frontal polymerization (FP) is an out-of-autoclave, self-sustaining cure process garnering significant adoption by enabling rapid and energy-efficient manufacture of FRPCs. Prior FP-based manufacture of FRPCs rely on in-plane triggers to initiate the reaction. In the present study, we adopt through-thickness curing of carbon FRPCs with emphasis on the energy input required and the resulting composite properties. High energy input resulted in high glass transition temperature (T_g = 156 °C), fiber volume fraction (V_f = 65%), and low void content ($V_v \approx 0$). Computational modeling and optimization complement the experiments with focus on further reducing the energy whilst maintaining the favorable properties achieved at high energy inputs. A 27.5% reduction in energy resulted while maintaining similar performance.

1. Introduction

Structural components in the transportation and energy sectors have increasingly integrated lightweight thermoset composites owing to their robust mechanical, thermal, and chemical properties [1–4]. Notwithstanding these benefits, the equipment, energy, and time requirements associated with the manufacturing of thermoset composites are costly and have long stunted market growth [5–9].

Strategies to reduce composite cure cycle time include snap-cure resins [10–13], heated substrates and molds [14–16], and frontal polymerization [17–25]. Snap-cure resins and heated substrates require constant application of external energy to achieve the necessary temperatures for cure, hence the part is limited by mold size and energy source. To mitigate these limitations optimization of the process parameters is necessary. To that effect, numerical modeling of the manufacturing process serves as a great tool for sweeping over process parameters, be it traditional bulk polymerization [26,27], or frontal polymerization [28–32]. An appropriate numerical optimization scheme can then be implemented to optimize the manufacturing process. To optimize traditional bulk-polymerization-based manufacturing, Rai and Pitchumani [33], and Li et al. [34] used gradient-based methods to design time-optimal autoclave cure cycles that reduce the cost and ensure that the manufactured part is fully cured and free of residual stresses. Alternatively, Dolkun et al. [35] implemented a multi-objective genetic algorithm to reduce the total cure time by 33% and reduce the thermal overshoot by 71%. In contrast to traditional methods, frontal polymerization is a self-sustaining curing strategy whereby polymerization occurs through propagation of a localized reaction front. The process is driven by the exothermic heat of polymerization, which substantially reduces the energy necessary to process thermoset polymers and composites [21]. Robertson et al. [22] frontally cured dicyclopentadiene (DCPD)/carbon fiber-reinforced polymer composites (FRPCs) using isolated edge triggers to propagate the front in the plane of the laminate (Fig. 1(a), (b)) as well as uniform heating on the bottom of the laminate (Fig. 1(c)) to trigger through-thickness propagation of the front. Centellas and coworkers [23] reported that multiple in-plane triggers (i.e., fronts) reduce cure times. Negative impacts of the merged interface were mitigated through application of pressure and heat.

Here, we investigate rapid through-thickness curing of carbon FRPCs using frontal-ring opening metathesis polymerization (FROMP),

* Corresponding author.
** Corresponding author at: Department of Materials Science Engineering, University of Illinois Urbana Champaign, Urbana, IL 61801, United States.
E-mail address: n-sottos@illinois.edu (N.R. Sottos).
[1] Equal contribution.

https://doi.org/10.1016/j.compositesa.2024.108084
Received 8 December 2023; Received in revised form 1 February 2024; Accepted 7 February 2024
Available online 9 February 2024

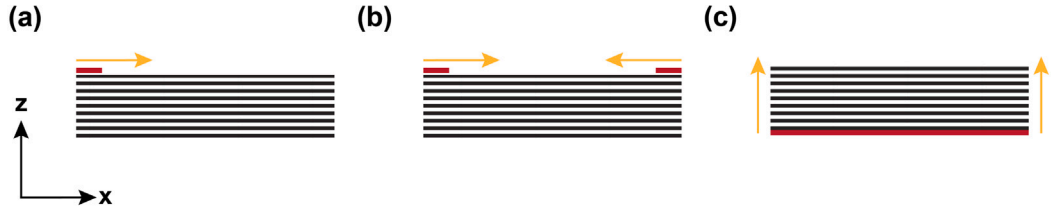

Fig. 1. Methods of initiating the FP-based curing of FRPCs | (a) One in-plane trigger; (b) two in-plane triggers; (c) through-thickness curing. Thermal triggers are shown in red with golden arrows indicating the direction of front propagation.

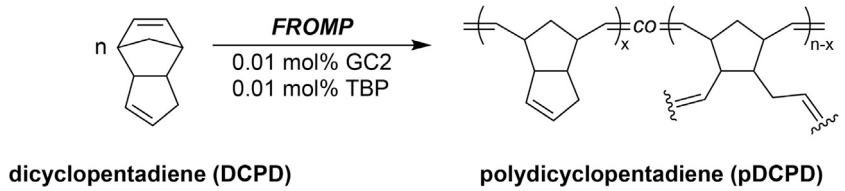

Fig. 2. FP resin chemistry | Application of an external thermal stimulus initiates frontal ring-opening metathesis polymerization of DCPD mixed with GC2 initiator and TBP inhibitor.

with emphasis on the energy input required and the resulting composite properties. Composite front characteristics (velocity and temperature), cure time–temperature, quality (fiber volume fraction, void content, uniformity), and performance (glass transition temperature and storage modulus) are evaluated for composites fabricated with varying energy input. The time–temperature cure behavior is modeled computationally and an adjoint-based optimization scheme [36] is implemented to reduce the energy required while maintaining the material performance. The optimal trigger profile is then validated experimentally.

2. Energy effect on composite manufacturing

2.1. Materials

Dicyclopentadiene (DCPD), 5-ethylidene-2-norbornene (ENB), second-generation Grubbs' catalyst (GC2), and tributyl phosphite (TBP) were purchased from Millipore-Sigma and used in the resin as received without further purification (Fig. 2). DCPD (Ultrene 99) was also purchased from Cymetech Corporation and used as received in the validation study (Section 4.2).

The DCPD was first melted in an oven at 50 °C, then mixed with 5 *wt.%* ENB to depress the melting point. The DCPD/ENB solution was then degassed at 100 kPa vacuum pressure overnight and is henceforth referred to as DCPD. In a separate container 62 g of DCPD (10,000 molar equivalents with respect to GC2) was combined with 13 μL of TBP (1 eq molar equivalent to GC2). An additional glass container with 40 mg of GC2 was sonicated while the DCPD solution was slowly introduced. The combined solution was sonicated for 15 min. Once prepared, the resin was infiltrated into the fabric preform. The reinforcement phase of the carbon FRPC consists of 12 plies of 10 cm × 12 cm Toray T300 carbon fabric (2 × 2 twill weave, tow size 3,000, areal density 204 g/m^2) (Rock West Composites, 13005-D-GROUP). Prior to the resin infiltration, the fabric was cut to the dimensions specified and heated at 120 °C for 1 hour to remove residual moisture. The fabric is then cooled in a desiccant box to ensure no moisture remains.

2.2. Vacuum-assisted resin transfer molding (VARTM)

Carbon-fiber-reinforced polymer composites were fabricated using single-bag vacuum-assisted resin transfer molding (VARTM) coupled with isostatic pressing (Fig. 3). The VARTM layup was prepared on a rigid nonconductive polytetrafluoroethylene (PTFE) substrate. A 12 cm × 15 cm resistive heating mat (Omega Engineering, SRFGA-506/10) was placed beneath the layup to initiate the reaction. A vacuum of 40 kPa was applied to the fabric preform then infused with the resin system. A second PTFE substrate was placed on the infused fabric preform. An external pressure of 308 kPa was applied by an isostatic press to consolidate the fabric preform resulting in a fiber volume fraction, V_f, of 65% with a desired thickness of 2.2 mm. FP was initiated using a thermal trigger from beneath the laminate. The target temperature, T_{target}, or the heating profile was specified for each sample based on the prescribed energy input.

2.3. Material characterization

Temperature Measurement, Front Velocity, and Energy Input: The temperature evolution during frontal curing was measured in-situ with T-type thermocouples (TMQSS, Omega) embedded at the bottom, mid-ply, and top surface of the fabric preform. The maximum temperature recorded by each thermocouple was defined as the maximum temperature, T_{max}, experienced by the laminate at that position. The front velocity, v_f, was determined by monitoring successive temperature peaks measured by the thermocouples. Experimental energy input for each laminate was determined by the heat flux of the heater and the duration of the prescribed heating, i.e., the start of the cooling step.

Void Content, V_v, and Fiber Volume Fraction, V_f : V_v of the cured composite was determined from polished cross-sections (20 mm) cut from the center of the panel. Polished samples were imaged with an optical digital microscope (VHX-5000, Keyence). ImageJ software was used to calculate the total void area relative to the cross-sectional area of the polished sample. The thickness of the specimen was measured by a micrometer, while the fiber volume fraction, V_f, was calculated using

$$V_f = \frac{f_A n}{\rho_f t}, \tag{1}$$

where f_A and ρ_f are the areal weight and fiber density of the fabric, respectively, n is the number of plies, and t is the panel thickness.

Dynamic Mechanical Analysis (DMA): The composite glass transition temperature, T_g, and the storage modulus, E', were determined by DMA. Rectangular specimens were cut from the composite panel and

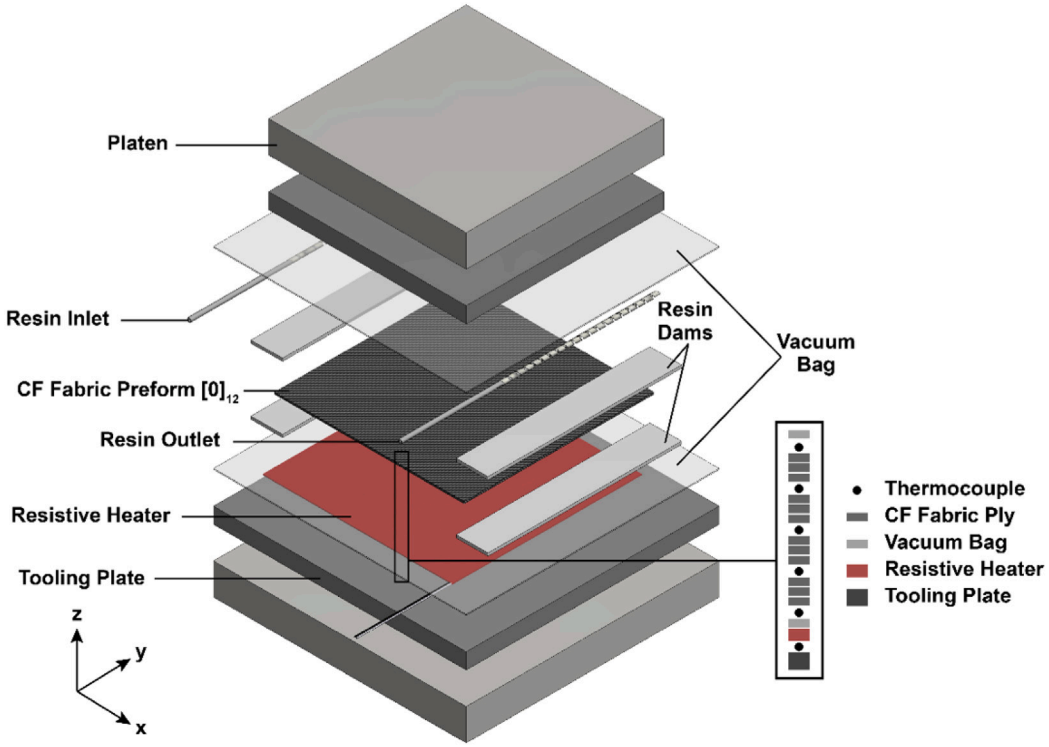

Fig. 3. Schematic set-up for through-thickness frontal curing | Exploded isometric view of a single-bag vacuum-assisted resin transfer molding (VARTM) coupled with isostatic pressing prepared on a PTFE tooling plate. The woven fabric preform is infused with liquid DCPD resin (x-direction) and consolidated (z-direction). Curing is then initiated by a resistive heater shown in red located below the composite panel.

polished to final dimensions of 44 mm × 5 mm × 2.2 mm. Samples were loaded on a three-point bend fixture with a span of 40 mm. A fixed force (2 N) with strain of 0.01% at a frequency of 1 Hz and a heating rate of 2 $\frac{°C}{min}$ from 0 °C to 250 °C were used for all samples. T_g was taken from the peak of the ratio of loss and storage modulus, $tan\,(\delta)$, using the TRIOS software analysis from TA Instruments.

2.4. Energy impact on composite properties

We systematically varied the energy input to the heater to achieve selected target maximum temperatures, (T_{target}), ranging from 77 °C to 193 °C, which, based on the maximum power output of the available heater and the area of the composite panel, translated to an energy input of 9 kJ to 48 kJ, respectively. The desired T_{target} was programmed into a custom proportional–integral–derivative (PID) controller that maintained the heating rate until the target was reached. Heating profiles associated with the two different methods of curing the laminate are shown in Fig. 4. The onset temperature, T_{onset}, is the temperature at which FP initiates. As the temperature increases beyond T_{onset}, the FP curing reaction dominates the heat generated until reaching a local maximum. After the peak, the sample either continues to heat to T_{target} (Method 2) or enters a cooling phase (Method 1).

The energy input has a positive correlation with T_{max} (Table 1), which is recorded by the thermocouple placed closest to the heater. We observe a monotonic increase in T_{max} with T_{target} up to T_{max} = 130 °C±2.78 °C at T_{target} = 193 °C. As the material preparation, infusion, and consolidation processes were the same for each laminate, V_f was maintained and V_v was mitigated at each T_{target}.

Composites processed with varying T_{target} were characterized by DMA (Fig. 5). For low T_{target} (77–155 °C), a small oscillation in E' is observed near T_g, which is likely due to the force-tracking features of the instrument coupled with undercuring in the laminate. Increasing the energy input into the system increases the T_g to 157 °C approaching T_g of the polymer (160 °C) [37]. At the highest target temperature, a notable increase in rubbery modulus occurs, likely related to complete curing of the resin. Despite the favorable increase in the properties, the energy required to cure the composite panel increased from 9 kJ to 48 kJ.

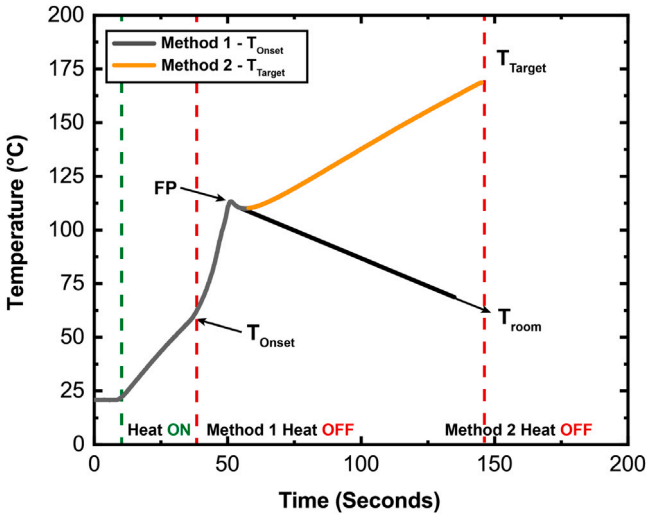

Fig. 4. Representative thermal curing profiles for through-thickness frontal curing | Two curing methods are adopted. In Method 1, heating is applied until the onset reaction temperature of the DCPD-based resin system is reached, relying solely on the monomer enthalpy. In Method 2, heating is applied beyond the observed FP reaction until a target temperature, T_{target}, is achieved, at which point the heating ceases.

3. Modeling and optimization of FP-based curing process

In this section we seek to determine the minimum energy required to cure the laminate whilst retaining the properties obtained at the higher energy input.

Table 1
Summary of composite curing characteristics and properties for the T_{target} survey. N=4. The uncertainty represents one standard deviation.

T_{target} (°C)	T_{max} (°C)	v_f (cm/min)	V_f (%)	V_v (%)	Energy input (kJ)
77	112 ± 1.00	1.24 ± 0.09	64.8 ± 1.2	0.05 ± 0.01	9
97	111 ± 0.55	1.11 ± 0.19	65.0 ± 0.4	0.03 ± 0.01	16
116	116 ± 0.45	1.29 ± 0.14	65.0 ± 0.4	0.03 ± 0.01	23
135	121 ± 0.74	1.25 ± 0.08	65.0 ± 0.4	0.04 ± 0.01	30
155	123 ± 1.65	1.27 ± 0.07	65.0 ± 0.4	0.03 ± 0.01	36
174	124 ± 2.88	1.21 ± 0.13	65.0 ± 0.4	0.04 ± 0.01	43
193	130 ± 2.78	1.20 ± 0.11	64.3 ± 1.1	0.04 ± 0.01	48

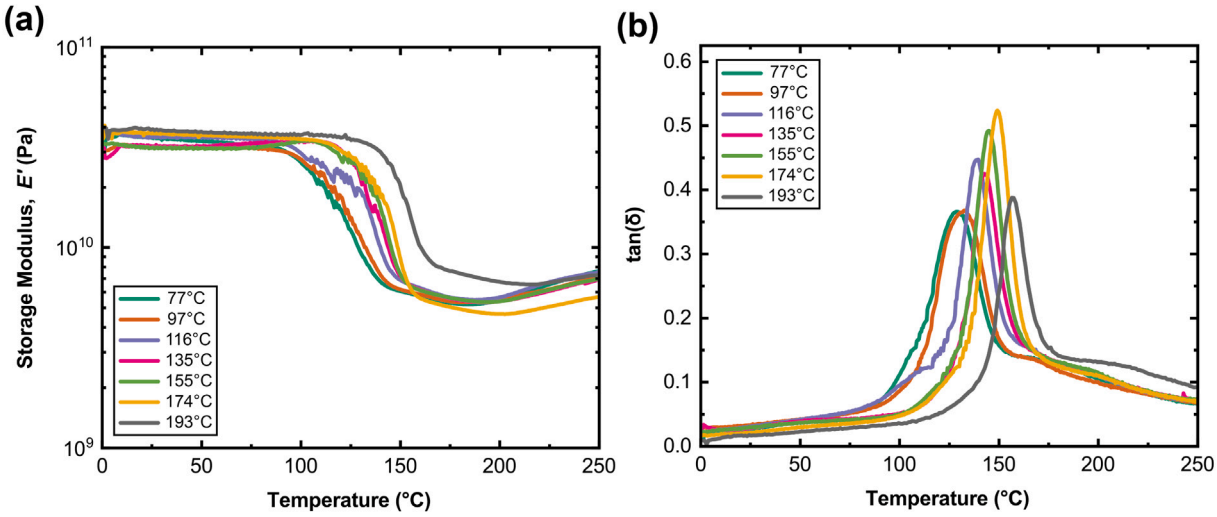

Fig. 5. DMA of FP carbon/pDCPD FRPCs | Carbon/pDCPD composites ($V_f = 65\%$) cured by through-thickness initiation of FP at varying T_{target} ranging from onset (77 °C) to high temperature cure (193 °C). (a) Characterization of the storage modulus, E', with temperature. (b) Ratio of storage and loss modulus or, $tan(\delta)$. Increase in T_{target} and consequently in the energy input for curing acts to increase the glass transition temperature.

3.1. Model formulation and implementation

For simplicity, the composite laminate and the top insulation are modeled in 1-D in the thickness direction (z) as shown in Fig. 6(a). As described in Section 2.2, the composite is 2.2 mm thick and the insulation is 1 *in* (25.4 mm) thick with the thermal trigger created by the heater placed at the bottom of the composite. FP in the composite and the heat losses to the insulation are modeled using the following reaction–diffusion relations:

$$\begin{cases} \overline{\rho C_p}\dfrac{\partial T}{\partial t} = \overline{\kappa_3}\dfrac{\partial^2 T}{\partial z^2} + \rho_m(1-\phi)H_r\dfrac{\partial \alpha}{\partial t}, \\ \dfrac{\partial \alpha}{\partial t} = A\exp\left(\dfrac{-E}{RT}\right)g(\alpha), \\ g(\alpha) = (1-\alpha)^n\alpha^m\left(\dfrac{1}{1+\exp(c_d(\alpha-\alpha_d))}\right), \quad \text{for } 0 \le z \le L_{comp} \\ \rho_i C_{p_i}\dfrac{\partial T}{\partial t} = \kappa_i\dfrac{\partial^2 T}{\partial z^2}, \quad \text{for } L_{comp} \le z \le L \end{cases} \tag{2}$$

where T (in K) is the temperature, α is the (non-dimensional) degree of cure, z (in m) is the spatial co-ordinate in the thickness direction, t (in s) is the time, H_r (in J/kg) is the enthalpy of the reaction, ϕ (set at 0.65) is the fiber volume fraction, and $\overline{\kappa_3}$ (in W/(m K)) and $\overline{\rho C_p}$ (in J/(m^3 K)) respectively denote the homogenized through-thickness thermal conductivity and volumetric heat capacity of the composite. The second and third equations describe the cure kinetics of the DCPD resin, where A (in $1/s$) is the time constant, E (in J/mol) is the activation energy, R (8.314 J/(mol K)) is the universal gas constant, n and m are the two exponents that define the order of the reaction in the Prout–Tompkins model [38], while c_d and α_d are the two non-dimensional constants introduced to include the effects of diffusion [39]. The final equation captures the temperature evolution in the insulation layer with ρ_i (in kg/m^3), C_{p_i} in (J/(kg K)), and κ_i denoting the density, specific heat capacity, and thermal conductivity of the insulation, respectively. The volumetric heat capacity of the composite is homogenized based on a simple rule of mixtures as

$$\overline{\rho C_p} = (1-\phi)(\rho C_p)_m + \phi(\rho C_p)_f, \tag{3}$$

where the subscripts m and f denote the matrix and the fibers, respectively. To determine the homogenized through-thickness thermal conductivity, we adopt the model proposed by Ning and Chou [40] (Eq. (16)), which yields $\overline{\kappa_3} = 0.38\ \frac{\text{W}}{\text{mK}}$. The material properties and cure kinetics parameters used in this work are listed in Tables 2 and 3, respectively. Eq. (2) is solved with the following initial and boundary conditions:

$$T(0 \le z \le L, 0) = T_0,\ \alpha\left(0 \le z \le L_{comp}, 0\right) = \alpha_0,$$
$$\begin{cases} -\overline{\kappa_3}\dfrac{\partial T}{\partial z}\cdot n(0,t) = Q^*(t), & \text{for } t \le t_{trig} \\ -\overline{\kappa_3}\dfrac{\partial T}{\partial z}\cdot n(0,t) = 0, & \text{for } t > t_{trig} \end{cases} \tag{4}$$

where T_0 is the initial temperature (set at 20 °C), α_0 is the initial degree of cure of the resin (set at 0.01), $Q^*(t)$ is the time-dependent heat flux trigger applied at the bottom of the domain, and t_{trig} is the duration of the trigger. Additionally, the temperature and heat flux are continuous at the composite/insulation interface. An example of a representative flux-time trigger profile used for the modeling is shown in Fig. 6(b).

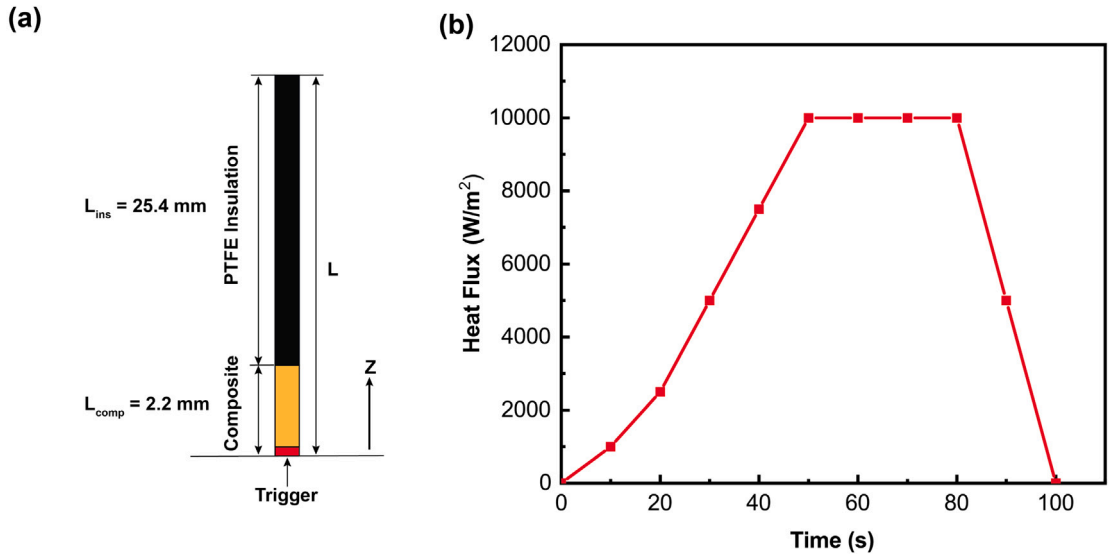

Fig. 6. Model geometry and applied heat flux profile | (a) 1-D computational domain comprising of the composite and the top insulation. FP is triggered in the composite by the application of a heat flux at the bottom of the domain. (b) Representative flux-time trigger profile. The trigger profile is a piecewise linear curve consisting of 10 linear segments of equal duration. The 11 end points (shown as symbols) defining the linear segments constitute the design variables in the optimization study described below.

Table 2
Thermal conductivity, density, and specific heat capacity of DCPD, carbon fibers, and PTFE insulation considered in this study.

	κ $(\frac{W}{mK})$	ρ $(\frac{kg}{m^3})$	C_p $(\frac{J}{kgK})$
DCPD	0.15	980.0	1600.0
Carbon fibers	10.45	1760.0	795.0
PTFE	0.03	2200.0	970.0

Table 3
Cure kinetics parameters of the Prout–Tompkins model Eq. (2) for DCPD.

n	m	c_d	α_d	A $(\frac{1}{s})$	E $(\frac{kJ}{mol})$	H_r $(\frac{J}{g})$
1.72	0.77	14.48	0.41	$8.55e+15$	110.75	365.0

The 1-D domain is discretized using 200 (100 elements for the composite and 100 elements for the insulation) linear finite elements resulting in the following semi-discrete system of equations for the composite domain:

$$\begin{bmatrix} [C_T] & -\rho_m(1-\phi)H_r[C_\alpha] \\ [0] & [C_\alpha] \end{bmatrix} \begin{Bmatrix} \dot{T} \\ \dot{\alpha} \end{Bmatrix} + \begin{bmatrix} [K_T] & [0] \\ [0] & [0] \end{bmatrix} \begin{Bmatrix} T \\ \alpha \end{Bmatrix} = \begin{Bmatrix} P_T \\ P_\alpha \end{Bmatrix}, \quad (5)$$

where $[C_\alpha] = \int N^T N dz$, $[C_T] = \int N^T \overline{\rho C_p} N dz$, $[K] = \int B^T \overline{\kappa_3} B dz$, $\{P_T\} = N^T Q^*(t)$, $\{P_\alpha\} = \int N^T A \exp(-\frac{E}{RT}) g(\alpha) dz$, $\dot{T} = \frac{\partial T}{\partial t}$, and $\dot{\alpha} = \frac{\partial \alpha}{\partial t}$. Here N refers to the vector of linear interpolation functions and B is the spatial derivative of N. Eq. (5) can be compactly written as

$$[\overline{C}] \left\{ \dot{\overline{U}} \right\} + [\overline{K}] \left\{ \overline{U} \right\} = \left\{ \overline{P} \right\}. \quad (6)$$

We then use the β-method as adopted by Zhu et al. [41] to obtain the fully discretized form of Eq. (6) expressed in a residual form as

$$\{R\}^n = \left[\frac{[\overline{C}]}{\Delta t} + \beta[\overline{K}] \right] \left\{ \overline{U} \right\}^n - \left[\frac{[\overline{C}]}{\Delta t} + (1-\beta)[\overline{K}] \right] \left\{ \overline{U} \right\}^{n-1} - \beta \left\{ \overline{P} \right\}^n - (1-\beta) \left\{ \overline{P} \right\}^{n-1}, \quad (7)$$

where $\left\{ \overline{U} \right\}^n$ and $\left\{ \overline{U} \right\}^{n-1}$ are the solution vectors at time steps n and $n-1$, respectively, and Δt (set at 0.05 s) is the time step. In this work, we adopt the Crank–Nicolson time-stepping scheme ($\beta = 0.5$) and use the Newton–Raphson method to solve the nonlinear algebraic equations at every time step. Since we use the inbuilt MATLAB function *fmincon* for the optimization study in Section 4.1, the code required for numerically integrating, assembling, and solving Eqs. (5)–(7) was developed in MATLAB.

3.2. Model validation

To validate the model, we selected the temperature–time trigger profile corresponding to $T_{target} = 193$ °C. As described in Section 2.3, the experimental setup involved 3 thermocouples placed through the thickness of the panel. To initiate the curing of the composite panel, the heater was run at full power till it reached a temperature of approximately 193 °C, after which it was turned off. The resulting heater temperature profile is presented in Fig. 7(a) as the solid black curve, together with the resulting experimental results recorded by the thermocouples being represented by the solid red, blue, and green curves. As apparent in that figure, the heater required approximately 190 seconds to reach a temperature of approximately 193 °C. To simulate this experiment numerically, we used the same heating profile (black curve) as a Dirichlet boundary condition applied at the bottom of the 1-D domain for a duration of $t_{trig} = 190$ seconds. After 190 s, the Dirichlet boundary condition was replaced by an insulated Neumann boundary condition. Adiabatic conditions were assumed at the top of the insulation layer. The numerical results are shown in Fig. 7(a) as the dashed red, blue, and green curves, corresponding to the top, mid, and bottom thermocouples, respectively. The numerical results show good agreement with their experimental counterparts for the heating and cooling phases, validating the numerical model. The model is also able to capture the onset of the FP characterized by the sudden temperature rise observed after approximately 40 s.

3.3. Optimization scheme

A benchmark for the energy cost was established by computing the energy associated with the temperature trigger shown in Fig. 7(a) by running a numerical simulation in the absence of reaction, i.e., by setting A to 0 in Eq. (5), thus eliminating the dependence of the diffusion equation on the heat released during the reaction. The flux associated

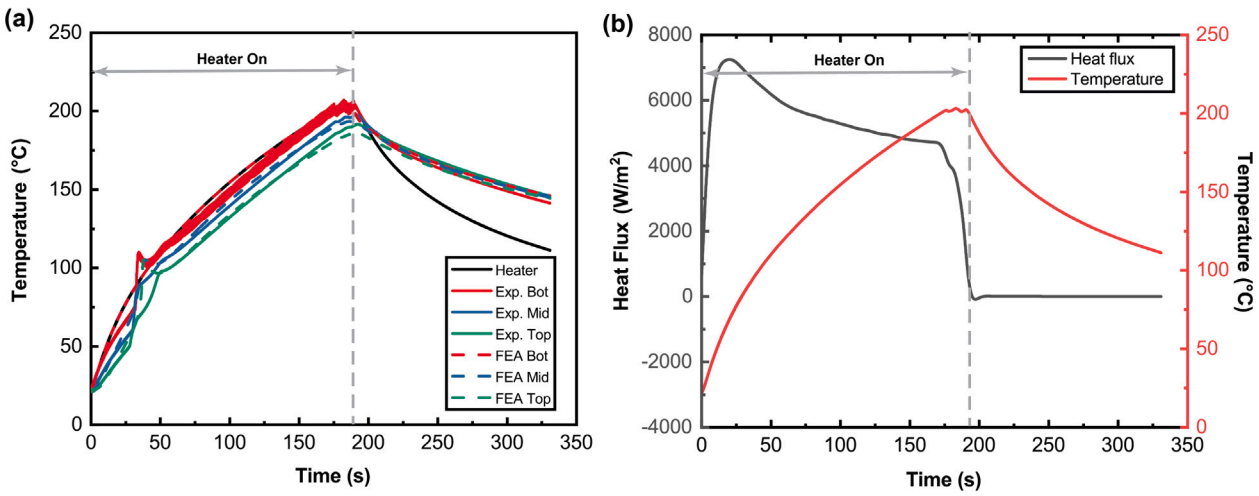

Fig. 7. Model validation for temperature prediction and heat flux extraction from temperature profile | (a) Comparison between numerical (dashed curves) and experimental (solid curves) results obtained by implementing the heater profile shown by the solid black curve. The numerical and experimental results show good agreement for the heating and cooling phases of the FP-based curing process. (b) Conversion of the experimental time–temperature trigger profile to a flux-time trigger profile to calculate the energy associated with the trigger.

with the experimental trigger was then computed by analyzing the bottom-most element and is shown in Fig. 7(b). The energy associated with the heater-on phase of the trigger was then computed as the product of the area under the flux-time curve (in J/m^2) from $t = 0$ to 190 s and the panel area (0.012 m^2), resulting in an energy cost of 12,231 J. As a result, we formulated our optimization objective as

$$minimize\ F := \frac{1}{E_0}\int_0^{t_f} -\overline{\kappa_3}\frac{\partial T}{\partial z}\cdot n(0,t)\,dt = \frac{1}{E_0}\int_0^{t_f} Q^*(t)dt, \tag{8}$$

where $Q^*(t)$ is the heat flux applied at the bottom of the domain, t_f is the duration of the applied thermal trigger, which for simplicity is assumed to be equal to the duration of the simulation, and E_0 is a scalar that depends on the initial guess for the optimization problem. The optimization constraint pertains to the final degree of cure, which must exceed a specified critical minimum value (α_{crit}) everywhere in the composite panel. Since the panel is heated from the bottom, the lowest value of the degree of cure is found at the top of the panel. Hence, for a computational domain with M degrees of freedom with the mth degree of freedom corresponding to the degree of cure for the top of the composite domain and the last time step ($t_f = N_t\Delta t$), the constraint takes the form

$$G := \{\omega\}^T\left(\{\alpha_{crit}\} - \left\{\overline{U}\right\}^{N_t}\right) \le 0, \tag{9}$$

where $\{\omega\}^T$ is an M-component row vector with a single non-zero entry corresponding to the mth degree of freedom, $\{\alpha_{crit}\}$ is an M-component column vector with all its entries being equal to α_{crit}, and $\left\{\overline{U}\right\}^{N_t}$ is the solution vector for the last time step.

As illustrated in Fig. 6(b), the flux-time trigger profile is represented as a piecewise linear curve comprised of 11 flux design variables ($[f_0(t_0), f_1(t_1), \ldots, f_{10}(t_{10})]$) that are equally spaced in time, resulting in the following definition for $Q^*(t)$:

$$Q^*(t) = f_i + \left(\frac{f_{i+1}-f_i}{t_{i+1}-t_i}\right)t, \text{ for } t_i \le t \le t_{i+1};\ i = 0, 1, \ldots, 10. \tag{10}$$

Next, we compute the sensitivities for the objective and constraint functions with respect to the design variables needed for the gradient-based optimization of the curing process. The expression of the sensitivities of the objective function with respect to the design variables is readily obtained as

$$\frac{dF}{df_i} = \frac{1}{E_0}\begin{cases}\dfrac{t_i - t_{i-1}}{2}, & \text{for } i = 1 \text{ and } 11\\ \dfrac{t_{i+1}-t_{i-1}}{2}, & \text{for } i = 2, 3, \ldots, 10.\end{cases} \tag{11}$$

To compute the gradients for the constraint function, we follow the method outlined in [36] and define a Lagrangian Π involving the constraint and the residual (Eq. (7)) as

$$\Pi = G + \sum_{n=1}^{N_t}\{\psi\}^{nT}\{R\}^n\left(\left\{\overline{U}\right\}^n, \left\{\overline{U}\right\}^{n-1}, f_i\right) = G, \tag{12}$$

where $\{\psi\}^{nT}$ is the transpose of the adjoint vector for the nth time step. It is essential to note that the above equation holds for any $\{\psi\}$ as the residual goes to 0 for each time step in the Newton–Raphson scheme. We then obtain the sensitivities for the constraint function by computing the gradients of the Lagrangian as

$$\begin{aligned}\frac{dG}{df_i} = \frac{d\Pi}{df_i} = \frac{\partial G}{\partial f_i} &+ \sum_{n=1}^{N_t}\left\{\frac{\partial G}{\partial\left\{\overline{U}\right\}^n}\right\}\left\{\frac{d\left\{\overline{U}\right\}^n}{df_i}\right\} + \sum_{n=1}^{N_t}\{\psi\}^{nT}\left\{\frac{\partial\{R\}^n}{\partial f_i}\right\}\\ &+ \sum_{n=1}^{N_t}\{\psi\}^{nT}\left\{\left[\frac{\partial\{R\}^n}{\partial\left\{\overline{U}\right\}^n}\right]\left\{\frac{d\left\{\overline{U}\right\}^n}{df_i}\right\}\right\}\\ &+ \sum_{n=1}^{N_t}\{\psi\}^{nT}\left\{\left[\frac{\partial\{R\}^n}{\partial\left\{\overline{U}\right\}^{n-1}}\right]\left\{\frac{d\left\{\overline{U}\right\}^{n-1}}{df_i}\right\}\right\}.\end{aligned} \tag{13}$$

Setting $n = N_t$ for the last time step and analyzing terms containing $\left\{\frac{d\left\{\overline{U}\right\}^{N_t}}{df_i}\right\}$, we obtain

$$\left\{\left\{\frac{\partial G}{\partial\left\{\overline{U}\right\}^{N_t}}\right\} + \{\psi\}^{N_t T}\left[\frac{\partial\{R\}^{N_t}}{\partial\left\{\overline{U}\right\}^{N_t}}\right]\right\}\left\{\frac{d\left\{\overline{U}\right\}^{N_t}}{df_i}\right\}. \tag{14}$$

To eliminate the dependence of the gradient on the term $\left\{\frac{d\left\{\overline{U}\right\}^{N_t}}{df_i}\right\}$, we set its coefficient to 0 and obtain Eq. (15)(a), which expresses the adjoint vector for the last time step. A similar analysis for an arbitrary

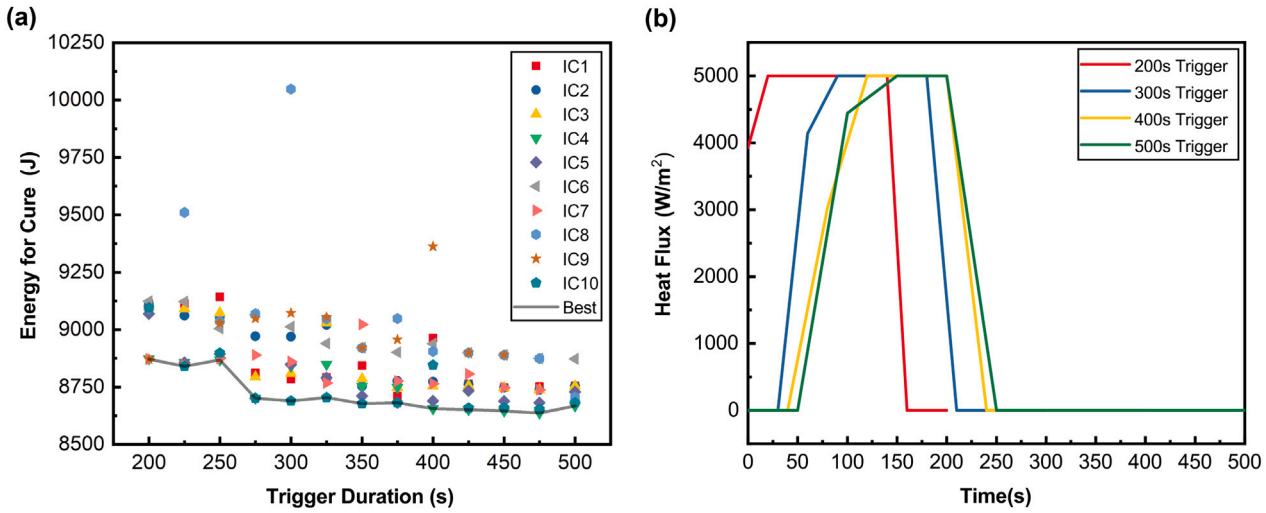

Fig. 8. Energy associated with the curing and flux profiles | (a) Energy associated with each trigger duration for the case $max(f_i) = 5000\ \frac{W}{m^2}$ obtained for 10 initial values of the design variables, showing the existence of local minima. The set of 'best' optimal solutions is denoted by the solid black curve. (b) Optimal flux-time trigger profiles obtained for trigger durations of 200 s, 300 s, 400 s, and 500 s.

time step n with $n < N_t$ yields Eq. (15)(b):

$$\{\psi\}^n = \begin{cases} -\left[\frac{\partial\{R\}^{N_t}}{\partial\left\{\overline{U}\right\}^{N_t}}\right]^{-T}\{\omega\} & \text{for } n = N_t, \\ -\left[\frac{\partial\{R\}^{n}}{\partial\left\{\overline{U}\right\}^{n}}\right]^{-T}\left[\frac{\partial\{R\}^{n+1}}{\partial\left\{\overline{U}\right\}^{n}}\right]^{T}\{\psi\}^{n+1} & \text{for } n < N_t. \end{cases} \quad (15)$$

Here $\left[\frac{\partial\{R\}^{N_t}}{\partial\left\{\overline{U}\right\}^{N_t}}\right]^{-T}$ and $\left[\frac{\partial\{R\}^{n}}{\partial\left\{\overline{U}\right\}^{n}}\right]^{-T}$ are the inverted and transposed Newton–Raphson Jacobian matrices for the last (N_t) and nth (such that $n < N_t$) time steps, respectively, and do not need to be recomputed, whereas $\left[\frac{\partial\{R\}^{n+1}}{\partial\left\{\overline{U}\right\}^{n}}\right]$ needs to be computed for each time step.

From Eq. (15), it is evident that the adjoint vector for time step n (with $n < N_t$) depends on the adjoint vector for time step $n + 1$. As a result, we compute the adjoint vectors backwards. It is also important to note that once computed, the adjoint vectors do not change for any of the design variables and that the same adjoint vectors are used to compute the gradients for all 11 design variables. Recall that the adjoint vectors are chosen such that they eliminate the dependence of the gradient on the terms $\left\{\frac{d\left\{\overline{U}\right\}^{n}}{df_i}\right\}$, leading to a simplification of Eq. (13) as

$$\frac{dG}{df_i} = \frac{d\Pi}{df_i} = \sum_{n=1}^{N_t}\{\psi\}^{nT}\left\{\frac{\partial\{R\}^{n}}{\partial f_i}\right\}, \quad (16)$$

where $\left\{\frac{\partial\{R\}^{n}}{\partial f_i}\right\}$ has to be computed on a case-by-case basis for each design variable.

To assess the accuracy of our adjoint gradient formulation, we compare the results from Eq. (16) to those obtained using a central finite-difference approximation. This verification study yielded a maximum relative error of less than 1%, proving the accuracy of the adjoint formulation. A similar procedure was adopted to verify the analytic gradients for the objective function (Eq. (11)), resulting in a relative error close to machine precision.

4. Process optimization

4.1. Computational optimization

As described earlier, the objective for the optimization is to minimize the energy associated with the flux-time trigger by minimizing the area under the trigger profile. This objective can be achieved by either lowering the maximum magnitude of the flux or by reducing the duration of the trigger. To study the effect of the maximum flux and the trigger duration on the optimal energy, we perform a process optimization analysis based on 3 values for the maximum flux (3000 $\frac{W}{m^2}$, 4000 $\frac{W}{m^2}$, and 5000 $\frac{W}{m^2}$) and 13 values of the trigger duration ranging from 200 s to 500 s in increments of 25 s. Additionally, since this optimization process involves local minima, we run each case with 10 different initial conditions resulting in a total of 390 optimization problems. These problems are solved by implementing the interior-point algorithm [42] using the inbuilt MATLAB function *fmincon* with the values of the design variables bound between $-0.001\ \frac{W}{m^2}$ and one of the aforementioned maximum flux values. For the constraint function, the value of α_{crit} is set at 0.99.

Fig. 8(a) shows the minimum energy obtained for the 130 optimization problems associated with a maximum applied flux value set to 5000 $\frac{W}{m^2}$. The variation in energy obtained for each trigger duration across the 10 initial trigger profiles indicates the presence of multiple local minima. To study the effects of the trigger duration on the energy for cure, we select the best results for each trigger duration (solid black curve in Fig. 8(a)). As illustrated by these optimal results, the required trigger energy decreases as the trigger duration increases from 200 s to 300 s and then remains almost constant with further increments in the trigger duration. From the optimal trigger profiles shown in Fig. 8(b), we attribute the initial drop in energy to the added freedom afforded due to the increase in the trigger duration. For triggers with a duration of 300 s and greater, we observe that the optimal trigger profiles are very similar except for the duration of the pre- and post-heating regions for which the applied flux is 0, leading to predicted optimized energy inputs that are independent of the trigger duration.

Fig. 9 compares the optimal solutions for the energy consumed for maximum flux values of 3000 $\frac{W}{m^2}$ (orange curve), 4000 $\frac{W}{m^2}$ (green curve), and 5000 $\frac{W}{m^2}$ (blue curve). As apparent there, the lowest energy costs are obtained for the case corresponding to a maximum applied flux of 5000 $\frac{W}{m^2}$. Additionally, due to the strict nature of the constraint, no feasible solutions exist for trigger durations of 200 s - 325 s for the case

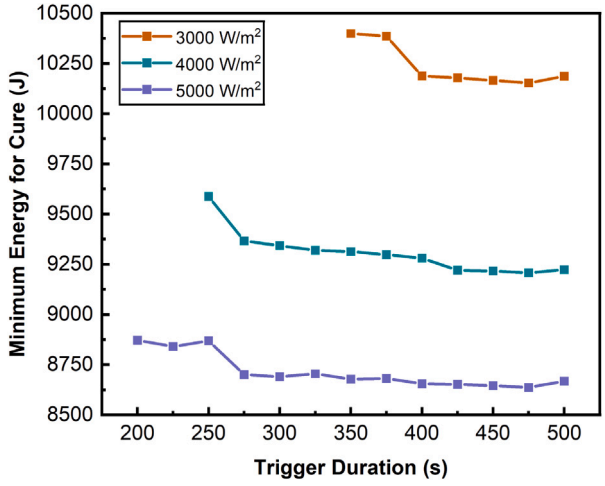

Fig. 9. Minimum energy for through-thickness frontal curing | Minimum energy predictions as a function of trigger duration for three values of the maximum applied heat flux.

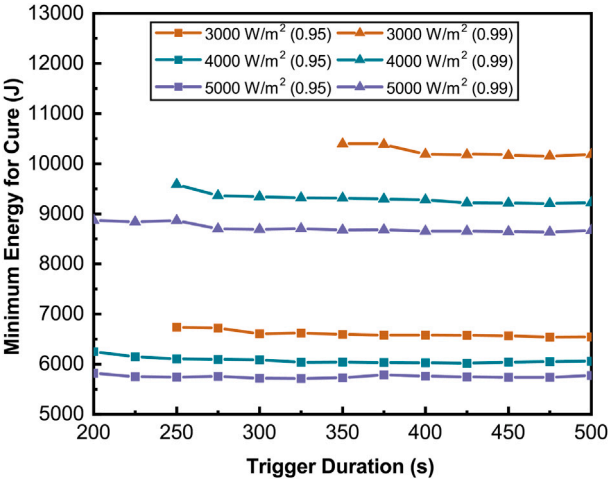

Fig. 10. Effect of critical degree of cure on predicted minimum energy | Comparison of the predicted energy as a function of trigger duration and maximum flux value for two values of α_{crit} : 0.99 (triangular symbols) and 0.95 (square symbols).

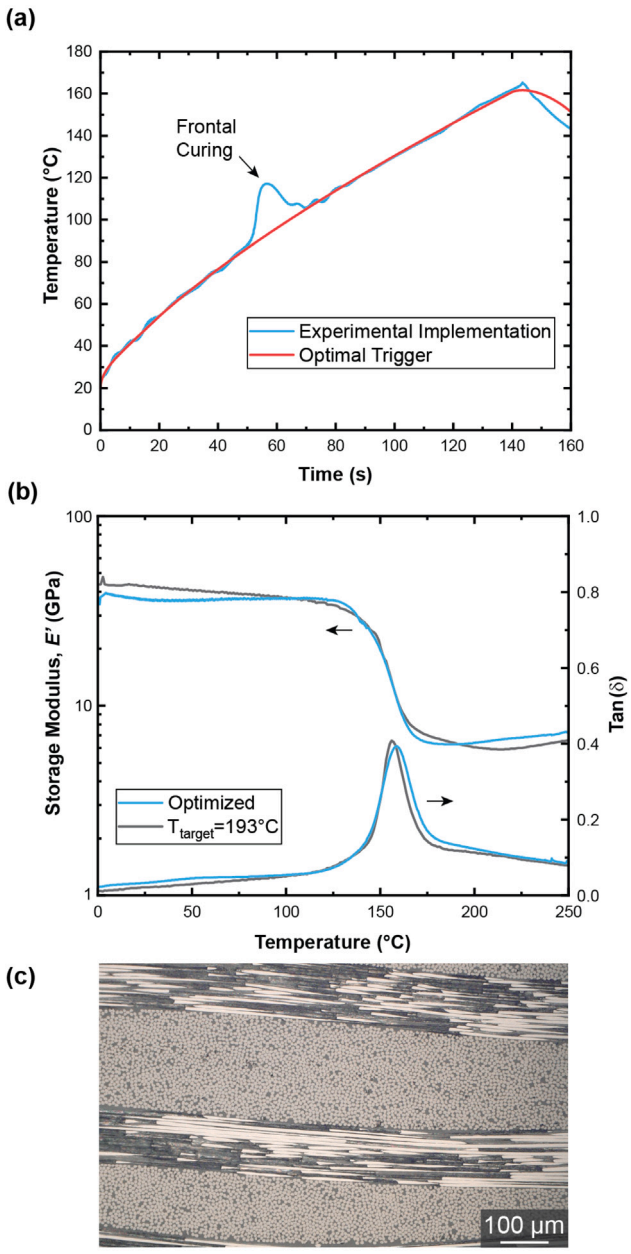

Fig. 11. Experimental implementation of optimal trigger | (a) Thermocouple trace associated with the experimental validation of the computationally obtained optimal trigger corresponding to 5000 $\frac{W}{m^2}$ and 200 s. (b) Thermomechanical response of the composite panel prepared by the optimized frontal curing process compared to that prepared with the original trigger cycle shown in Fig. 7(a). (c) A representative optical micrograph of the composite panel manufactured using the optimized frontal curing process.

of 3000 $\frac{W}{m^2}$, and for trigger durations of 200 s - 225 s for the case of 4000 $\frac{W}{m^2}$.

The choice of the α_{crit} constraint has a substantial impact on the optimization process, as shown in Fig. 10 for the cases $\alpha_{crit} = 0.99$ (triangular symbols) and $\alpha_{crit} = 0.95$ (square symbols). The results indicate that the minimum energy input obtained for all combinations of maximum flux and trigger duration values are significantly lower for $\alpha_{crit} = 0.95$ than for $\alpha_{crit} = 0.99$. Additionally, as α_{crit} decreases, optimum solutions satisfying the constraint can be found for a wider range of trigger durations for maximum flux values of 3000 and 4000 $\frac{W}{m^2}$.

4.2. Implementation of optimized curing process

To validate the predicted optimized curing cycle, we experimentally implement the optimized thermal profiles corresponding to a maximum applied heat flux of 5000 $\frac{W}{m^2}$ and a 200 s trigger selected based on the available heater and power supply. We manually adjust the voltage to match the numerically predicted temperature evolution shown as the red curve in Fig. 11(a). The experimental implementation, shown in blue, closely matches the numerical curve. The temperature spike associated with FP is also illustrated by the experimental curve. The carbon/pDCPD composite panel cured frontally using the optimized trigger profile is compared to that processed with $T_{target} = 193$ °C. The thermomechanical properties of the composite made with the initial and optimized trigger profiles are very similar as shown in Fig. 11(b). Optical micrographs (Fig. 11(c)) of the composite specimens show similar microstructures and void contents. The micrographs of the optimally cured laminate also show a few plies did not nest well and the laminate was likely infused with excess resin, leading to resin rich regions and a slightly lower V_f than the laminates presented in Table 1.

Table 4
Comparison of composite curing characteristics and properties. The uncertainty represents one standard deviation.

Cure case	V_f (%)	V_v (%)	Energy input (kJ)
$T_{target} = 193°C$	64.3 ± 1.1	0.04 ± 0.01	12.2
Optimal Trigger	59.7 ± 2.1	0.17 ± 0.16	8.9

The difference in V_f is not unexpected given human variations in layup and infusion techniques and is not a result of the optimized thermal trigger (see Table 4).

5. Conclusions

In this work, we have utilized through-thickness frontal polymerization to manufacture carbon/pDCPD FRPCs with varying target temperatures and energy inputs. T_{target} = 193 °C achieved the highest front temperatures and thermomechanical properties, i.e., high glass transition temperature and uniform modulus. However, the energy input required to cure the laminate to achieve these properties was substantially higher than in-plane FP-based manufacturing. Computational modeling and optimization of the frontal curing process has predicted a thermal trigger profile that produced desirable properties and reduced the energy input. The optimized thermal trigger profile has been validated experimentally and has been shown to achieve properties comparable to those obtained for the best case T_{target} = 193 °C while reducing the energy input by about 27.5%.

CRediT authorship contribution statement

S. Vyas: Writing – review & editing, Writing – original draft, Software, Formal analysis, Conceptualization. **N.A. Parikh:** Writing – review & editing, Writing – original draft, Methodology, Formal analysis, Conceptualization. **T.C. Price:** Writing – review & editing, Validation, Methodology. **D.P. Patel:** Data curation. **T.B. Le:** Data curation. **P.H. Geubelle:** Writing – review & editing, Supervision. **N.R. Sottos:** Writing – review & editing, Supervision, Funding acquisition.

Declaration of competing interest

Nil Parikh reports financial support was provided by Arnold and Mabel Beckman Foundation. Nancy Sottos reports financial support was provided by National Science Foundation. Nancy Sottos reports financial support was provided by Air Force Office of Scientific Research. If there are other authors, they declare that they have no known competing financial interests or personal relationships that could have appeared to influence the work reported in this paper.

Data availability

Data will be made available on request.

Acknowledgments

The authors acknowledge the support of the NSF LEAP HI Program, United States (Grant #1933932) as well as support from the AFOSR Center for Excellence on Self-Healing, Regeneration, and Structural Remodeling, United States (Award FA9550-20-1-0194). N.A.P. also thanks the Arnold and Mabel Beckman Foundation, United States for financial support.

References

[1] Daniel I, Ishai O. Engineering mechanics of composite materials, vol. 1994, Oxford university press New York; 2006.
[2] Brøndsted P, Lilholt H, Lystrup A. Composite materials for wind power turbine blades. Annu Rev Mater Res 2005;35:505–38.
[3] Friedrich K, Almajid A. Manufacturing aspects of advanced polymer composites for automotive applications. Appl Compos Mater 2013;20(2):107–28.
[4] Karbhari V, Seible F. Fiber reinforced composites–advanced materials for the renewal of civil infrastructure. Appl Compos Mater 2000;7(2):95–124.
[5] Kluge N, Lundström T, Ljung A, Westerberg L, Nyman T. An experimental study of temperature distribution in an autoclave. J Reinf Plast Compos 2016;35(7):566–78.
[6] Abliz D, Duan Y, Steuernagel L, Xie L, Li D, Ziegmann G. Curing methods for advanced polymer composites-a review. Polymers Polymer Composites 2013;21(6):341–8.
[7] Witik R, Gaille F, Teuscher R, Ringwald H, Michaud V, Månson J. Economic and environmental assessment of alternative production methods for composite aircraft components. J Clean Prod 2012;29:91–102.
[8] Bader MG. Selection of composite materials and manufacturing routes for cost-effective performance. Composites A: Appl Sci Manuf 2002;33(7):913–34.
[9] of America Department of Energy US. Chapter 6 - innovating clean energy technologies in advanced manufacturing. 2015.
[10] Malnati P, Sloan J. Fast and faster: Rapid-cure resins drive down cycle times. 2018, Composites World.
[11] Hexion Inc. Epoxy systems for automotive structural components. 2019.
[12] Advanced materials araldite LY 3031®/Aradur 3032®. 2015.
[13] 750 S. Chapter 6 - innovating clean energy technologies in advanced manufacturing. 2020.
[14] Silcock M, Garschke C, Hall W, Fox B. Rapid composite tube manufacture utilizing the quicksteptm process. J Compos Mater 2007;41(8):965–78.
[15] Agius S, Magniez K, Fox B. Cure behaviour and void development within rapidly cured out-of-autoclave composites. Composites B 2013;47:230–7.
[16] Davies L, Day R, Bond D, Nesbitt A, Ellis J, Gardon E. Effect of cure cycle heat transfer rates on the physical and mechanical properties of an epoxy matrix composite. Compos Sci Technol 2007;67(9):1892–9.
[17] Ruiu A, Sanna D, Alzari V, Nuvoli D, Mariani A. Advances in the frontal ring opening metathesis polymerization of dicyclopentadiene. J Polym Sci A 2014;52(19):2776–80.
[18] Sangermano M, D'Anna A, Marro C, Klikovits N, Liska R. UV-activated frontal polymerization of glass fibre reinforced epoxy composites. Composites B 2018;143:168–71.
[19] Sangermano M, Antonazzo I, Sisca L, Carello M. Photoinduced cationic frontal polymerization of epoxy–carbon fibre composites. Polym Int 2019;68(10):1662–5.
[20] Tran A, Koch T, Knaack P, Liska R. Radical induced cationic frontal polymerization for preparation of epoxy composites. Composites A 2020;132:105855.
[21] Goli E, Parikh N, Yourdkhani M, Hibbard N, Moore J, Sottos N, et al. Frontal polymerization of unidirectional carbon-fiber-reinforced composites. Composites A 2019;105689.
[22] Robertson I, Yourdkhani M, Centellas P, Aw J, Ivanoff D, Goli E, et al. Rapid energy-efficient manufacturing of polymers and composites via frontal polymerization. Nature 2018;557(7704):223.
[23] Centellas P, Yourdkhani M, Vyas S, Koohbor B, Geubelle P, Sottos N. Rapid multiple-front polymerization of fiber-reinforced polymer composites. Composites A 2022;158:106931.
[24] Naseri I, Yourdkhani M. Rapid and energy-efficient frontal curing of multifunctional composites using integrated nanostructured heaters. ACS Appl Mater Interfaces 2022.
[25] Li Q, Shen H, Liu C, Wang C, Zhu L, Chen S. Advances in frontal polymerization strategy: From fundamentals to applications. Prog Polym Sci 2022;127:101514.
[26] White S, Kim C. A simultaneous lay-up and in situ cure process for thick composites. J Reinf Plast Compos 1993;12(5):520–35.
[27] Kim C, Teng H, Tucker C, White S. The continuous cuing process for thermoset polymer composites. Part 1: modeling and demonstration. J Compos Mater 1995;29(9):1222–53.
[28] Goli E, Robertson I, Agarwal H, Pruitt E, Grolman J, Geubelle P, et al. Frontal polymerization accelerated by continuous conductive elements. J Appl Polym Sci 2019;136(17):47418.
[29] Chen Z, Ziaee M, Yourdkhani M, Zhang X. Multiphysics modeling of frontal polymerization-assisted layer-by-layer additive manufacturing of thermoset polymer components. Addit Manuf 2022;59:103182.
[30] Wang Y. Modeling the through-thickness frontal polymerization of unidirectional carbon fiber thermoset composites: Effect of microstructures. J Appl Polym Sci 2022;139(31):e52735.
[31] Chen Z, Zhang X. Manufacturing multifunctional vascularized composites by through-thickness frontal polymerization and depolymerization: A numerical study on the impact of sacrificial fiber configurations. Compos Sci Technol 2023;110394.

[32] Tarafdar A, Jia C, Hu W, Hosein I, Fu K, Wang Y. Three-dimensional modeling of frontal polymerization for rapid, efficient, and uniform thermoset composites manufacturing. Composites B 2023;266:111029.
[33] Rai N, Pitchumani R. Optimal cure cycles for the fabrication of thermosetting-matrix composites. Polym Compos 1997;18(4):566–81.
[34] Li M, Zhu Q, Geubelle P, Tucker III C. Optimal curing for thermoset matrix composites: thermochemical considerations. Polym Compos 2001;22(1):118–31.
[35] Dolkun D, Zhu W, Xu Q, Ke Y. Optimization of cure profile for thick composite parts based on finite element analysis and genetic algorithm. J Compos Mater 2018;52(28):3885–94.
[36] James K, Waisman H. Topology optimization of viscoelastic structures using a time-dependent adjoint method. Comput Methods Appl Mech Engrg 2015;285:166–87.
[37] Ivanoff D, Sung J, Butikofer S, Moore J, Sottos N. Cross-linking agents for enhanced performance of thermosets prepared via frontal ring-opening metathesis polymerization. Macromolecules 2020;53(19):8360–6.
[38] Kessler M, White S. Cure kinetics of the ring-opening metathesis polymerization of dicyclopentadiene. J Polym Sci A 2002;40(14):2373–83.
[39] Yang G, Lee J. Curing kinetics and mechanical properties of endo-dicyclopentadiene synthesized using different grubbs' catalysts. Ind Eng Chem Res 2014;53(8):3001–11.
[40] Ning Q, Chou T. A closed-form solution of the transverse effective thermal conductivity of woven fabric composites. J Compos Mater 1995;29(17):2280–94.
[41] Zhu Q, Geubelle P, Li M, Tucker III C. Dimensional accuracy of thermoset composites: Simulation of process-induced residual stresses. J Compos Mater 2001;35(24):2171–205.
[42] Byrd R, Hribar M, Nocedal J. An interior point algorithm for large-scale nonlinear programming. SIAM J Optim 1999;9(4):877–900.